Chapter 6

Emergence of dielectric properties by doping of semi-transition metal in semiconductor complex perovskite oxide

6.1. Introduction

The class of semiconductor materials that display high dielectric constant and low tangent loss, and demonstrate these properties independent of frequency and temperature independent, are used to construct microelectronic devices for capacitor applications, placing them in the category of ideal materials [1]. Dielectric capacitors differ from electrochemical capacitors in that they have less self-discharged and more heat stability [2]. Therefore, these materials have great potential for utilization in high-power applications like energy systems, commercial power systems, medical equipment, and variety of sensing devices [3]. A suitable dielectric material, CCTO ($CaCu_3Ti_4O_{12}$) ceramic has a high dielectric permittivity at 1 kHz and 25 °C [4, 5]. It is widely accepted that an Internal Barrier Layer Capacitance (IBLC) model is the basic cause of the giant dielectric response [6, 7]. Several methods have been used in investigations of the grain boundaries of CCTO materials [8, 9]. The IBLC hypothesis, which holds that a significant intrinsic potential barrier existed at the CCTO grain boundaries, is supported by S. Y. Chung's proof of the insulator- semiconductor junction assumption. For the gigantic dielectric permittivity, several theoretical models have received widespread acceptance, although they are still debatable [10]. By dramatically lowering tangent loss and raising the dielectric constant, there are several ways to enhance the dielectric characteristics of CCTO for use in capacitor applicators. The production of highly capacitive ceramics with low dielectric loss has been investigated via the replacement of metal ions into the lattice. Dopants have been employed in several researches to enhance the non-Ohmic and dielectric characteristics of CCTO ceramics. The Cu^{2+} and Ti^{4+} sites of the

CCTO structure have been replaced with a variety of dopants, including Mg^{2+}, Zn^{2+}, Sn^{4+}, Zr^{4+}, and W^{6+}. Rare reports of Ge^{4+} substitution in

the Ti^{4+} sites of CCTO ceramics exist. By doping CCTO ceramics with Ge^{4+}, extremely high dielectric constant (10^5) and minimal tangent loss (0.064-0.068) at 1 kHz and 25°C were achieved when x was raised from 0 to 0.10, of the ceramic $CaCu_3Ti_{4-x}Ge_xO_{12}$ while the tangent loss was noticeably reduced. The resultant tangent loss, however, is still more than 0.06 [11]. The first significant issue for practical usage in electrical and energy storage applications is the relatively high dielectric loss and low resistivity of CCTO ceramic. Researchers have tried a variety of methods to reduce the tangent loss of ceramics to address this serious issue. It is expected that the co-substitution of doping ions may boost the dielectric and/or nonlinear electrical responses in the CCTO structure. Many scientists have tried to figure out how to dope this ceramic composite system with metal ions like $Zn^{2+}$and Sn^{4+} to raise the dielectric constant value. Many $ACu_3Ti_4O_{12}$ (A= Ca, Sr, $Bi_{2/3}$, $Bi_{1/2}Na_{1/2}$, $La_{2/3}$, etc.) class of oxides have been identified in recent years, and it has been established that they display enormous dielectric capabilities. Similar to CCTO, BCTO ($Bi_{2/3}Cu_3Ti_4O_{12}$) ceramic has BCC (Body Centered Cubic) structure [12]. According to P. Gautam et al., The BCTO ceramic, sintered at 1173 K for 8 h, has a high dielectric constant (= 2.9 x 10^4) at 323 K and 100 Hz, which was also effectively synthesized as a powder using the sol-gel method, and when it was sintered for 20 h at 1273 K with this approach, was 1.1 x 10^4 and tangent loss was 0.11 at 1 kHz [13]. Therefore, deeper comprehension of the physical characteristics of BCTO is required to understand the doping impact of metal ions in BCTO.

$Bi_{2/3}Cu_3Ti_{4-x}Ge_xO_{12}$ and $Bi_{2/3}Cu_{3-x}Zn_xTi_{4-x}Ge_xO12$ (where x=0.05) ceramics were created in the present study using the semi-wet method. The microstructure, dielectric, and electrical

characteristics were examined and presented in the result and discussion part of this manuscript.

6.2. Material Synthesis and Characterization

Semi-wet synthesis was used to create BCTGO-0.05 and BCZTGO-0.05, also known as $Bi_{2/3}Cu_3Ti_{4-x}Ge_xO_{12}$ and $Bi_{2/3}Cu_{3-x}Zn_xTi_{4-x}Ge_xO_{12}$ (where x= 0.05), respectively. First, the following ingredients were measured in stoichiometric amounts: Bismuth nitrate $Bi(NO_3).5H_2O$ (99% Merck, India), Copper acetate $(CH_3COO)_2Cu.H_2O$ (99% Merck, India), Zinc acetate $(CH_3COO)_2Zn.H_2O$(98% Merck, India), Titanium (IV) oxide TiO_2(98.5% Merck, India), glycine (99.5%, Merck India),and Germanium (IV) oxide GeO_2 (99.99 % Merck, India). Double distilled water was used to dissolve $Bi(NO_3)_3.5H_2O$, $Cu(CH_3COO)_2.H_2O$, $GeO_2$and $Zn(CH_3COO)_2.H_2O$. Then, solid TiO_2 was added to this solution in a stoichiometric proportion. The predetermined quantity of citric acid (99.5%, Merck India) was added to aforementioned solution to operate as a complexing agent. The obtained solutionwas heated on hotplate magnetic stirrer at 343–353 K to remove water with subsequent stirring. The dry powders of BCTGO-0.05 and BCZTGO-0.05 were produced after the removal majority of the gases by self-ignition process. The resultant powders were then processed via pestle and mortar to create fine powders. The obtained powder was calcined at 1073 K for 8 h.5 tons of pressure was applied over 90 s by a hydraulic press to create cylindrical pellets. Pellets were made using PVA (as a binder) and heated for 3 h at 773 K. In the end, pellets of BCTGO-0.05 and BCZTGO-0.05 were created and sintered for 8 h at 1123 K.

Using X-ray diffractometer (Rigaku miniflex 600, Japan), the phase formation of the prepared materials were checked. Scanning electron microscopy (ZEISS model, EVO-18

research, Germany) and energy-dispersive X-ray spectroscopy (Oxford instruments, Great Britain) were used to analyze the microstructure and elements of all samples respectively. Transmission Electron Microscopy (TEM, FEI Tecnai-20G) was used to get Bright Field TEM pictures. XPS (X-ray Photoelectron Spectroscopy)was used to validate the oxidation state of the elements found in the ceramics. The pellet surfaces were silver coated for dielectric measurements, and dielectric data were collected using an LCR meter (PSM 1735-NumetriQ, Newton 4th Ltd. UK) in 300-500 K temperature range and 100 Hz- 1 MHz frequency range. We bought iso-propanol, Nafion solution, and acetylene black (AB) from Alfa Aesar. By combining 5 mg of active material, 0.625 mg of AB, 0.2 mL of isopropanol, and 12 L of Nafion, the individual electrode was created. Glossy carbon paper with an area of 1 cm^2 was impregnated with the dispersion, which was then allowed to dry under normal atmospheric conditions. Silver glue, which functioned as a current collector, joined copper wire to the electrode. The different electrochemical characteristics of the manufactured electrodes were assessed using Versastat 3. Utilizing a three-electrode mechanism, electrochemical impedance spectroscopy (EIS) and cyclic voltammetry (CV) were performed on the constructed systems. The working electrode (fabricated system/active material), the reference electrode (Ag/AgCl), and the counter electrode (Platinum) made up the three-electrode system. The working electrode in the three-electrode setup has a mass loading of 2 mg/cm^2. The stable potential range was determined as -0.2 V to 0.8 V using CV graphs that were recorded at a rate of 5 mV/s. At a 10 mV AC amplitude, the three-electrode setups underwent EIS. The electrolyte used for the electrochemical tests was a 1M KOH solution.

6.3 Results and Discussion

6.3.1. X-ray Diffraction (XRD)

The Phase development of BCTGO-0.05 and BCZTGO-0.05 ceramics were seen in the X-ray diffraction pattern, as illustrated in Fig. 6.1. XRD peaks of these ceramics, which are identical to BCTO (JCPDS card no. 46-0725), are identified as (2 0 0), (2 1 1), (2 2 0), (3 1 0), (2 2 2), (3 2 1), (4 0 0), (3 3 0), (4 2 0), (4 2 2), (4 4 0), (5 3 0), (6 0 0) and (6 1 1) planes. The crystallite size (D) of the ceramics BCTGO-0.05 and BCZTGO-0.05 were determined by using the Debye-Scherrer formula [14], which is given below in equation (6.1):

$$D = \frac{k\lambda}{\beta\cos\theta} \qquad (6.1)$$

Where k is the crystal shape coefficient (k=0.89), λ is the wavelength used in XRD, β is the Full-Width Half Maximum (FWHM) and θ is the diffraction angle. For the ceramics BCTGO-0.05 and BCZTGO-0.05, the average crystallite size was determined as 39.52 nm and 46.32 nm, respectively. The lattice parameter (a) for BCTGO-0.05 and BCZTGO-0.05 ceramics were calculated as 7.413Å and 7.408 Å respectively. The lattice volume of BCTGO-0.05 and BCZTGO-0.05 ceramics were determined as 407.3634$Å^3$ and 406.6157 $Å^3$ respectively.

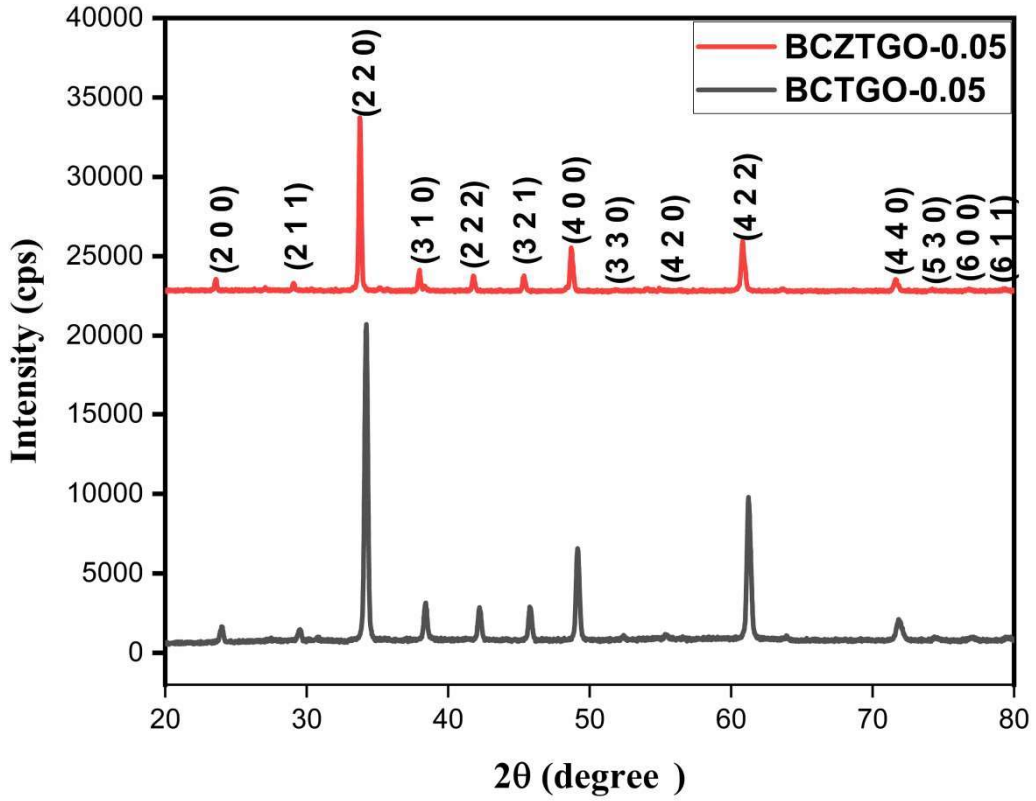

Fig. 6.1 XRD Pattern of BCTGO-0.05 and BCZTGO-0.05 ceramics sintered at 1123 K for 8 h.

6.3.2. Scanning Electron Microscopic (SEM) Studies

SEM images of BCTGO-0.05 and BCZTGO-0.05 ceramics are depicted in Fig. 6.2a and b, respectively. Zn and Ge ion doping in BCTO ceramics directly affects the way that ceramics develop. Some porosity may be noticed in the SEM images figure. The burning of citric-nitrate precursor gel may have caused gas evolution, which might be the cause of the porosity. The pictures also make it evident that grains are found in granular form, with polygonal shapes that are clearly divided by grain borders. As seen in the pictures, particle aggregation happens when Zn and Ge are doped in BCTO ceramics. Ceramics made using

BCTGO-0.05 and BCZTGO-0.05 were found to have average grain sizes of 0.62 µm and 0.68 µm, respectively.

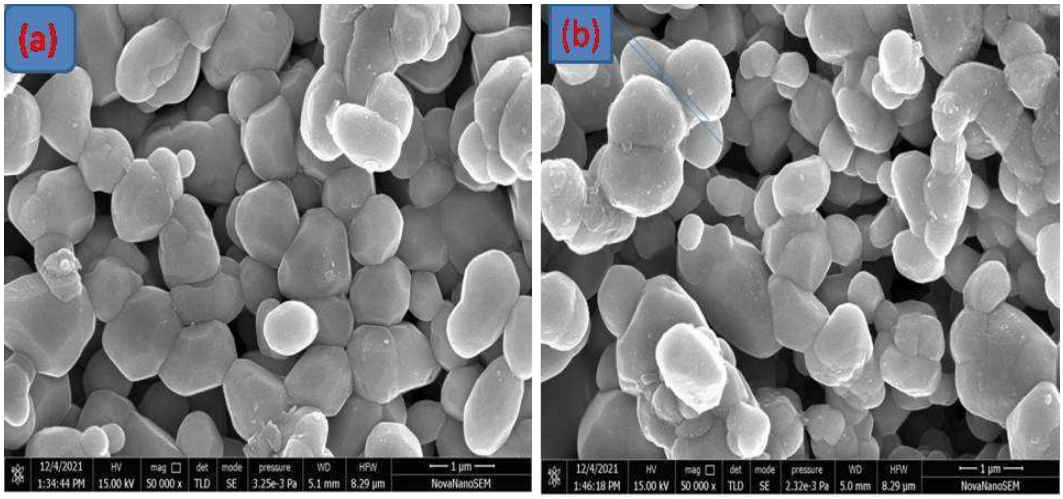

Fig. 6.2 SEM images of (a) BCTGO-0.05 and (b) BCZTGO-0.05 ceramics sintered at 1123 K for 8 h.

The EDX spectra of the ceramics BCTGO-0.05 and BCZTGO-0.05 are shown in Fig. 6.3a and b, respectively. EDX data were used to analyze the stoichiometry and purity of all the samples. The atomic % and weight % of Bi, Cu, Ti, Ge and O were 4.52, 20.92, 27.70, 0.34, 46.52 and 21.62, 30.43, 30.35, 0.57, 17.03 respectively, which gives a formula close to $Bi_{2/3}Cu_3Ti_{3.95}Ge_{0.05}O_{12}$ (i.e. BCTGO-0.05).

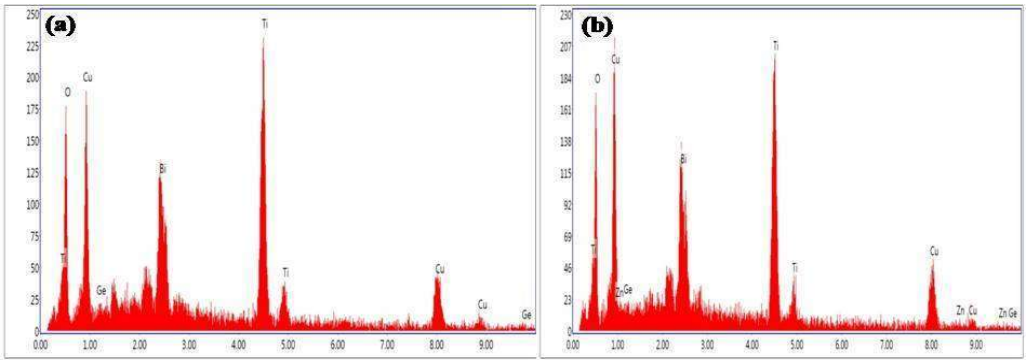

Fig. 6.3 EDX images **(a)** BCTGO-0.05 and **(b)** BCZTGO-0.05 ceramics sintered at 1123 K for 8 h.

The atomic % and weight % of Bi, Cu, Zn, Ti, Ge, O are 4.46, 20.34, 0.32, 27.52, 0.33, 47.03 and 21.48, 29.79, 0.48, 30.36, 0.51, 17.38 respectively, which gives a formula close to $Bi_{2/3}Cu_{2.95}Zn_{0.05}Ti_{3.95}Ge_{0.05}O_{12}$ (i.e., BCZTGO-0.05). Thus, Stoichiometry of all samples was confirmed by EDX data.

6.3.3. Transmission Electron Microscopic (TEM) Studies

Fig. 6.4 displays the bright-field TEM micrographs along with the SAED patterns of the ceramics BCTGO-0.05 and BCZTGO-0.05. The bright-field TEM data displayed in Fig. 6.4a, b were used to compute the particle size. For BCGTO-0.05, and BCZTGO-0.05 ceramics, it was found as 99 ± 5 nm, 112 ± 10 nm, respectively using Image J software. Due to particle agglomeration, it is shown that particle size rises as Zn concentration is added in BCTGO-0.05 ceramic [15]. Fig. 6.4 (a), (b) demonstrated the crystalline character of the particles.

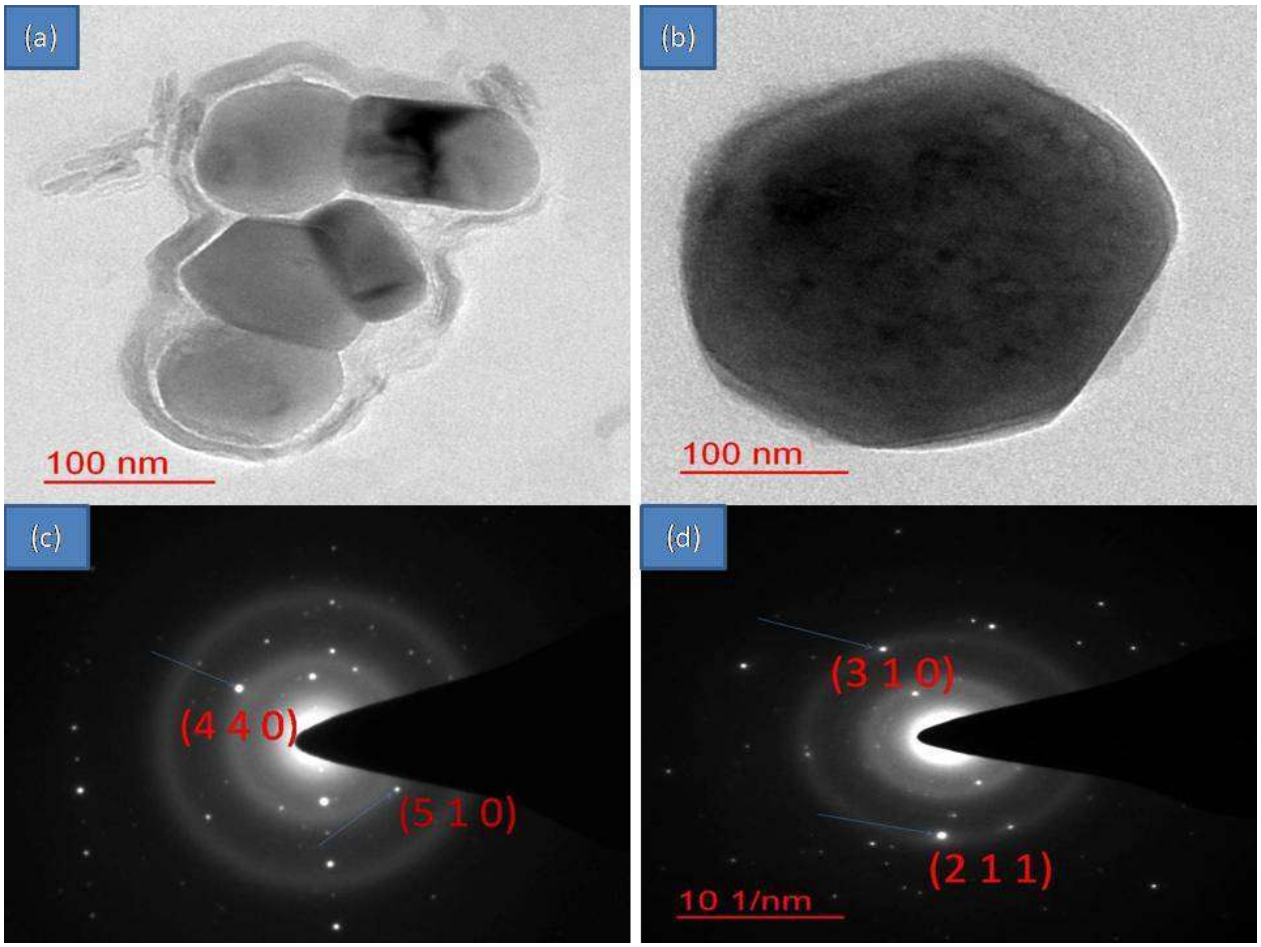

Fig. 6.4 (a), (b) TEM images and (c), (d) SAED pattern of BCTGO-0.05 and BCZTGO-0.05 ceramics sintered at 1123 K for 8 h respectively.

Fig. 6.4c, d demonstrates the Selected Area Electron Diffraction (SAED) patterns of BCTGO-0.05, and BCZTGO-0.05 sintered ceramics respectively. The crystal planes of the ceramics were obtained from the SAED pattern. The incidence of the bright spot of the SAED pattern demonstrated the nano-crystalline nature of particles.

6.3.4. X-Ray Photoelectron Spectroscopic (XPS) Studies

X-Ray Photoelectron Spectroscopy (XPS) Studies have verified the oxidation states of the elements found in the BCTGO-0.05 and BCZTGO-0.05 ceramics. Fig. 6.5 displays the XPS spectrum of BCTGO-0.05 ceramic. The XPS spectra of this ceramic, which contain the elements Bi, Cu, Ti, Ge, and O are displayed in Fig. 6.5a, b, c, d, and e, respectively.

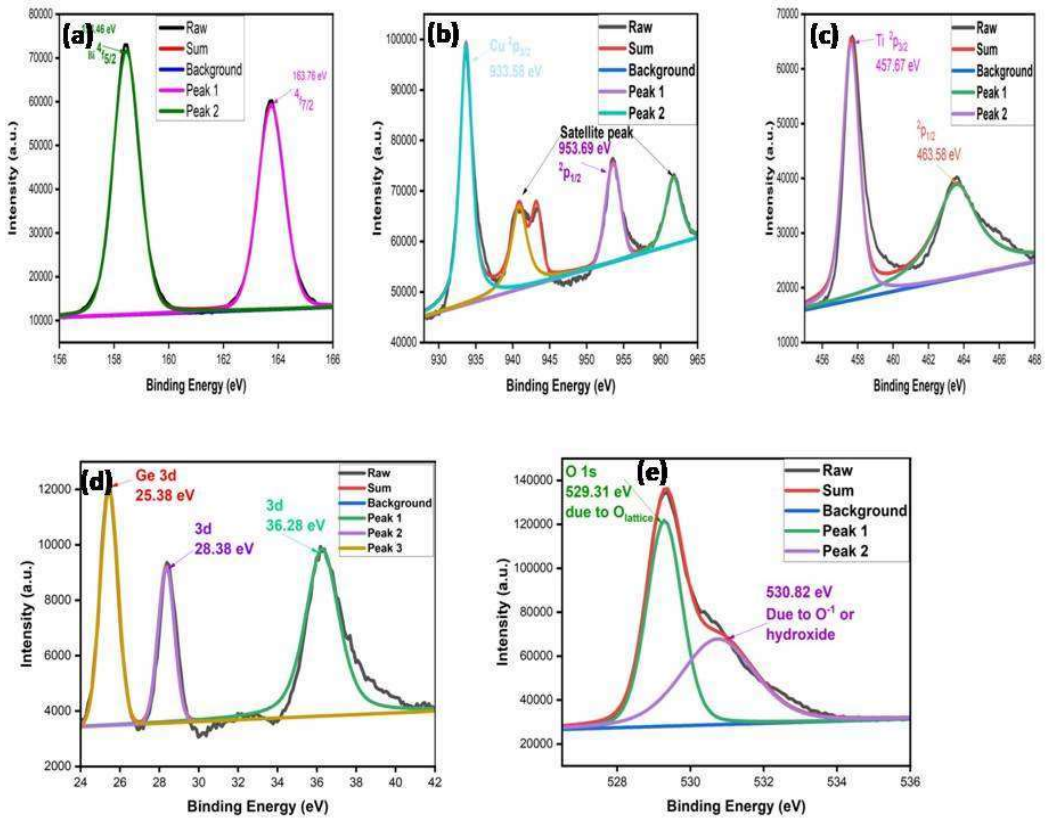

Fig. 6.5 XPS spectra of (a) Bi, (b) Cu, (c) Ti, (d) Ge, and (e) O of BCTGO-0.05 ceramic sintered at 1123 K for 8 h.

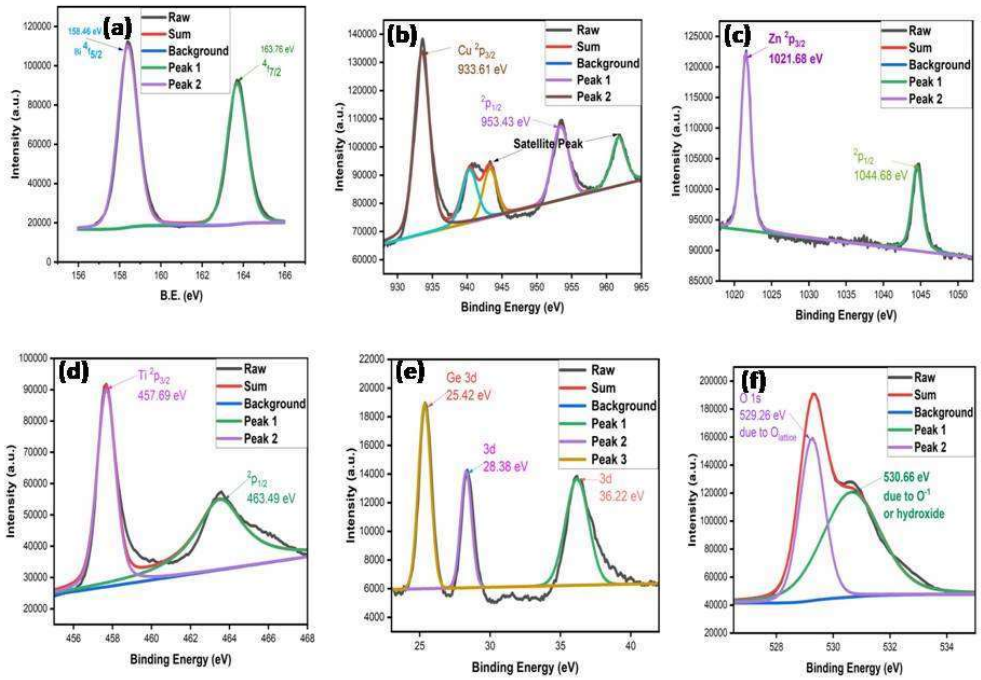

Fig. 6.6 XPS spectra of (a) Bi, (b) Cu, (c) Zn, (d) Ti, (e) Ge, and (f) O of BCZTGO-0.05 ceramic sintered at 1123 K for 8 h.

Two peaks in Fig. 6.5a that correlate to Bi $^4f_{5/2}$ and Bi $^4f_{7/2}$, respectively, with binding energies of 158.46 and 163.76 eV, support the existence of Bi^{3+}. Peak locations for Cu, Ti, O, and Ge has seen in Fig.5b, c, d, and e support their respective oxidation states of +2, +4, -2, and +2 [16]. Fig. 6.6 displays the XPS spectrum of BCZTGO-0.05 ceramic. The XPS spectra of this ceramic, which contain the elements Bi, Cu, Zn, Ti, Ge, and O are displayed in Fig. 6.6a, b, c, d, e, and f respectively.

Two peaks in Fig. 6.6a that correlate to Bi $^4f_{5/2}$ and Bi $^4f_{7/2}$, respectively, with binding energies of 158.46 and 163.76 eV, support the existence of Bi^{3+}. Peak locations for Cu, Zn,

Ti, Ge, and O has seen in Fig. 6.6b, c, d, e, and f support their respective oxidation states of +2, +2, +4, +4, and -2 [17,18].

6.3.5. Dielectric Studies

The relationship between the dielectric permittivity and frequency for the ceramics BCTGO-0.05 and BCZTGO-0.05 is exhibited in Fig. 6.7a and b respectively at selected temperatures. The fluctuation in dielectric permittivity with the frequency seen in the picture is nearly the same for both ceramics. In conclusion, the dielectric constant (ε_r) exhibits higher value in low-frequency region, whereas it drops with increasing frequency and becomes constant in higher frequency zone. Space charge polarization takes place in the low frequency range. In the higher frequency region, quick periodic reversal phenomena of the electric field occur, which prevent ions from diffusing in the direction of electric field [19, 20]. The dielectric constants of BCTGO-0.05 and BCZTGO-0.05 ceramics were 563 and 265 respectively at 423 K and 100 Hz.

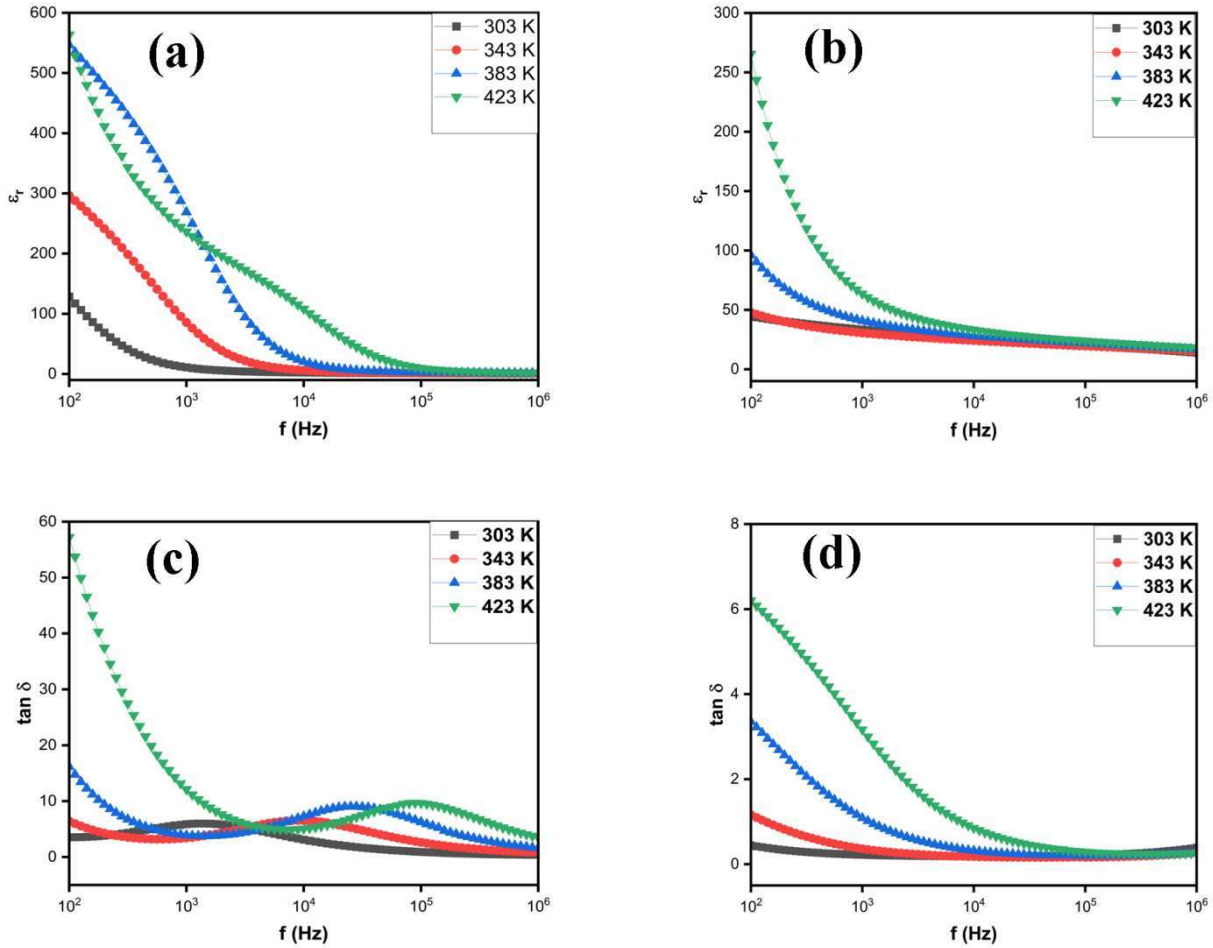

Fig. 6.7 Frequency dependence of dielectric constant(ε_r) of (a) BCTGO-0.05 and (b) BCZTGO-0.05; Frequency dependence of dielectric loss (tan δ) for (c) BCTGO-0.05 and (d) BCZTGO-0.05 ceramics at few selected temperatures.

Fig. 6.7cand d display the fluctuation of tan δ with frequency for the BCTGO-0.05 and BCZTGO-0.05 ceramics respectively at few selected temperatures. The relaxation peaks were observed in BCTGO-0.05 and BCZTGO-0.05 ceramics The BCZTGO-0.05 has the lowest dielectric loss (0.18). The tan δ values of BCTGO-0.05 and BCZTGO-0.05 ceramics are found as 3.12 and 0.18 respectively at 303 K and 10 kHz. Fig. 6.8a and b display the dielectric constant (ε_r) vs. temperature (T) graph of the BCTGO-0.05 and BCZTGO-0.05

ceramics respectively at few selected temperatures. It is concluded that the ε_r does not change up to 350 K and after that, it increases with increase in temperature.

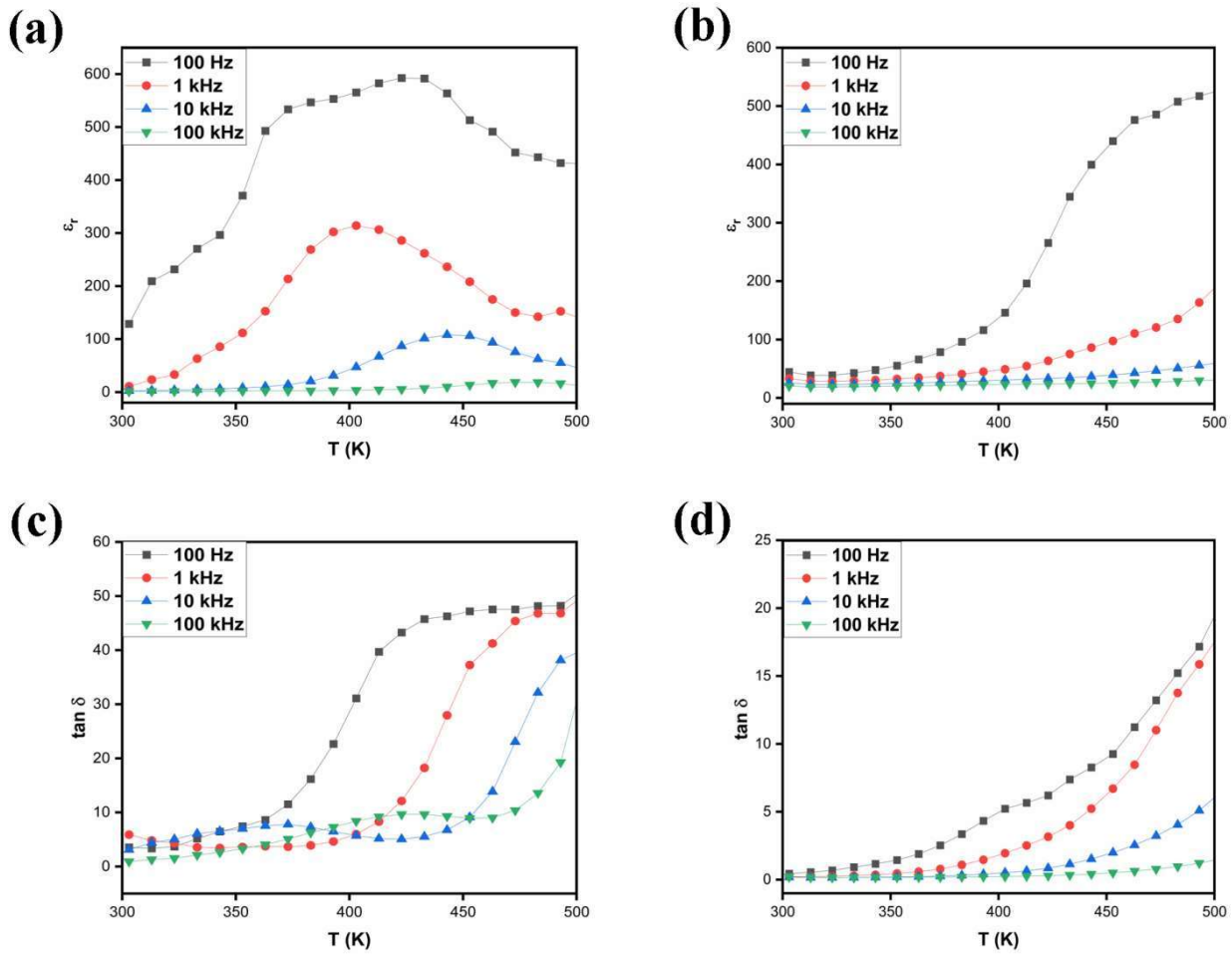

Fig. 6.8 Temperature dependence of dielectric constant (ε_r) of (a) BCTGO-0.05 and (b) BCZTGO-0.05; Frequency dependence of dielectric loss (tan δ) for (c) BCTGO-0.05 and (d) BCZTGO-0.05ceramics at few selected frequencies.

Fig. 6.8c and d show tan δ vs. T graphs for BCTGO-0.05 and BCZTGO-0.05 ceramics at few selected frequencies. The variation of tan δ with T shows similar behavior as graph of ε_r vs. T. It is observed that BCTGO-0.05 ceramic exhibited the lowest tangent loss.

6.3.6. Impedance Spectroscopic Studies

The correlation of the imaginary impedance (Z″) with change in frequency at specific temperatures has been revealed in Fig. 6.9a and b for BCTGO-0.05 and BCZTGO-0.05 ceramics respectively. With increasing frequency, the value of Z″ decreases in the higher frequency regions and It was been collapse to each other. Two relaxation peaks were appeared at all measured temperatures in case of BCTGO-0.05 sample. The first relaxation peak in the lower frequency region was obtained due to the electrode phenomenon and another peak was observed due to the grain boundaries effect. It shows the emergence of relaxation peaks.

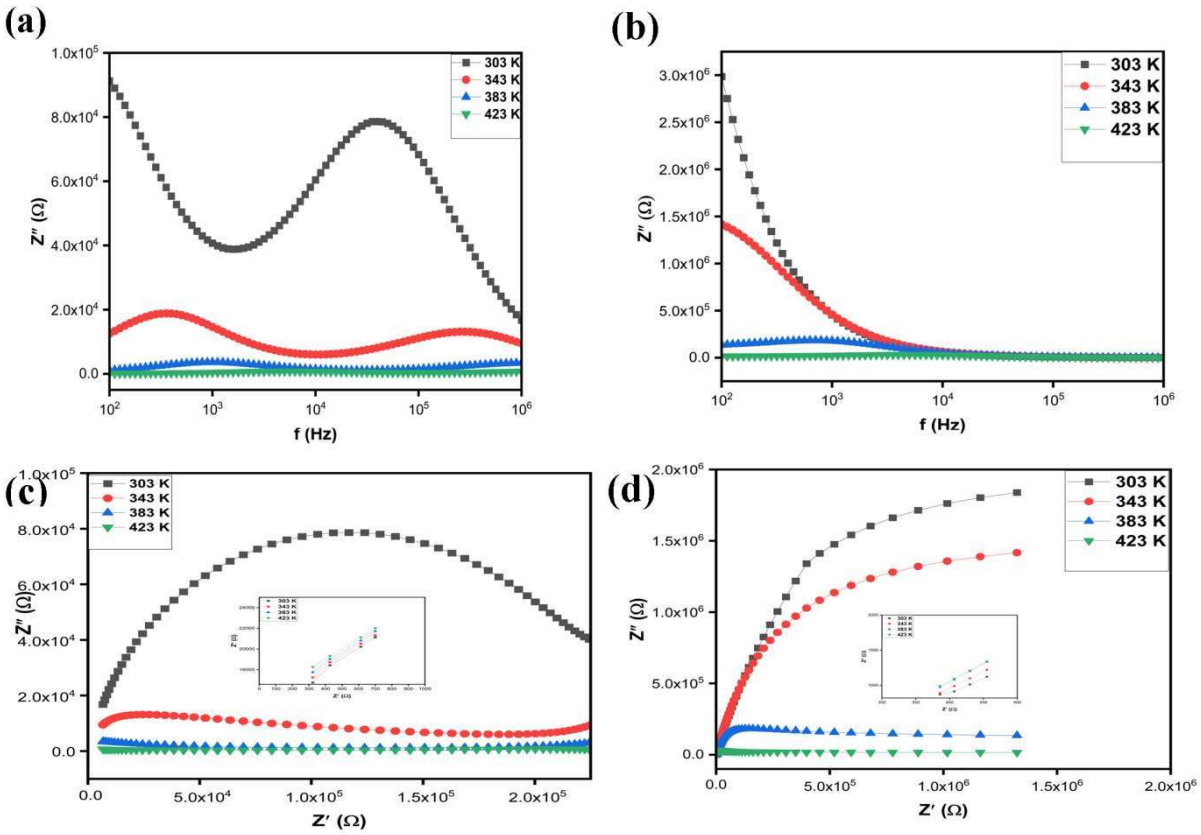

Fig. 6.9 frequency dependence of imaginary part of impedance (Z″) of (a) BCTGO-0.05 and

(b) BCZTGO-0.05; Complex impedance plot (Z″ vs Z′) of (c) BCTGO-0.05 and (d) BCZTGO-0.05 ceramics at few selected temperatures.

The relaxation behavior of ceramics were observed. Z″ vs Z′ plot at few selected temperatures of BCTGO-0.05 and BCZTGO-0.05 ceramics are shown in Fig. 6.9c and d. The semicircular arc is seen in both samples indicating the effect of the grain boundary. Due to the higher value of grain boundary resistance, the semicircular arcs for grains get reduced at high frequency. The grain resistance is determined with the help of inset figures, recorded in the high-frequency region. The value of grain resistances at 303 K, 343 K, 383 K, and 423 K are calculated as 310 Ω, 290 Ω, 240 Ω, and 180 Ω respectively for BCTGO-0.05 ceramic. The value of grain resistances at 303 K, 343 K, 383 K, and 423 K are calculated as 380 Ω, 375 Ω, 365 Ω, and 355 Ω respectively for BCZTGO-0.05 ceramic. It is seen that the resistance of grain along with the grain boundaries are semiconducting [21].

6.3.7. Electrical Conductivity

Fluctuation of ln σ vs 1000/T (K^{-1}) at selected frequencies of BCTGO-0.05 and BCZTGO-0.05 ceramics are given in Fig. 6.10a and b respectively. It can be concluded from the figure that the conductivity behavior of the ceramics linearly increase with increase in temperature. The temperature dependence of conductivity is governed by Arrhenius law. From electrical conduction data, the activation energy has been calculated the slope of the plot of ln σ vs 1000/T. The calculated activation energy is found as 0.47, 0.38, 0.37, and 0.35 eV at 100 Hz, 1 kHz, 10 kHz, and 100 kHz respectively for BCTGO-0.05 ceramic. The calculated activation energy is found as 0.54, 0.49, 0.39, and 0.36 eV at 100 Hz, 1 kHz, 10 kHz, and 100 kHz respectively for BCTGO-0.05 ceramic. It was observed in both samples that the

activation energy slows down on raising frequency. This occurs because of the improvement of electronic jumps on increasing the applied frequency, which is responsible for hopping charge carrier mechanism.

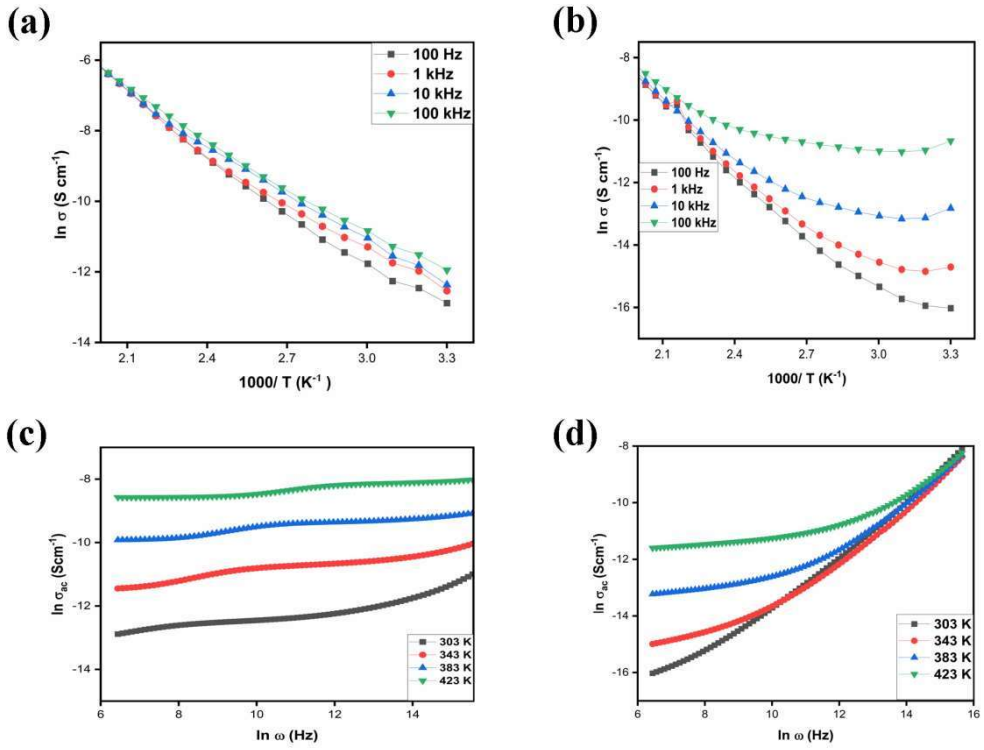

Fig. 6.10 Plots of Conductivity (ln σ) with the inverse of the temperature of (a) BCTGO-0.05 and (b) BCZTGO-0.05; frequency dependence of AC conductivity of (c) BCTGO-0.05 and (d) BCZTGO-0.05 ceramics

The variation of AC conductivity with frequency for BCTGO-0.05 and BCZTGO-0.05ceramics are shown in Fig. 6.10c, d respectively. The frequency-dependent conductivity can be described by the Jonscher power law [31].

$$\sigma(\omega)=\sigma_0+A\omega^s \qquad (6.2)$$

Where A is a constant and s is the power-law exponent.

The AC conductivity [22, 23] mainly depends on frequency. The power-law exponent (s) was estimated from the slope of the curve ln σ vs. ln ω for BCTGO-0.05 and BCZTGO-0.05 ceramics. It is determined as 0.48, 0.17, 0.16, and 0.14 at 303 K, 343 K, 383 K, and 423 K respectively for BCTGO-0.05 ceramics. It is calculated as 0.92, 0.84, 0.61, and 0.51 at303 K, 343 K, 383 K, and 423 K respectively for BCZTGO-0.05 ceramics. The temperature dependence of the dielectric conduction process is related to the hopping -charge mechanism [24]. The conduction mechanism can be illustrated by the thermally activated hopping process in BCTGO-0.05 and BCZTGO-0.05 ceramics over the potential barrier at the grain boundary.

6.3.8. Cyclic Voltammetry

Cyclic Voltammetry results (Fig. 6.11a) show that in the case of BCZTGO-0.05 more current is generated than BCTGO-0.05. So, it can be concluded that BCZTGO-0.05 has more conducting nature than BCTGO-0.05. There is no significant redox peak for both materials. The plateaus are non-rectangular, which reflect the pseudo capacitive behavior of the materials [25].

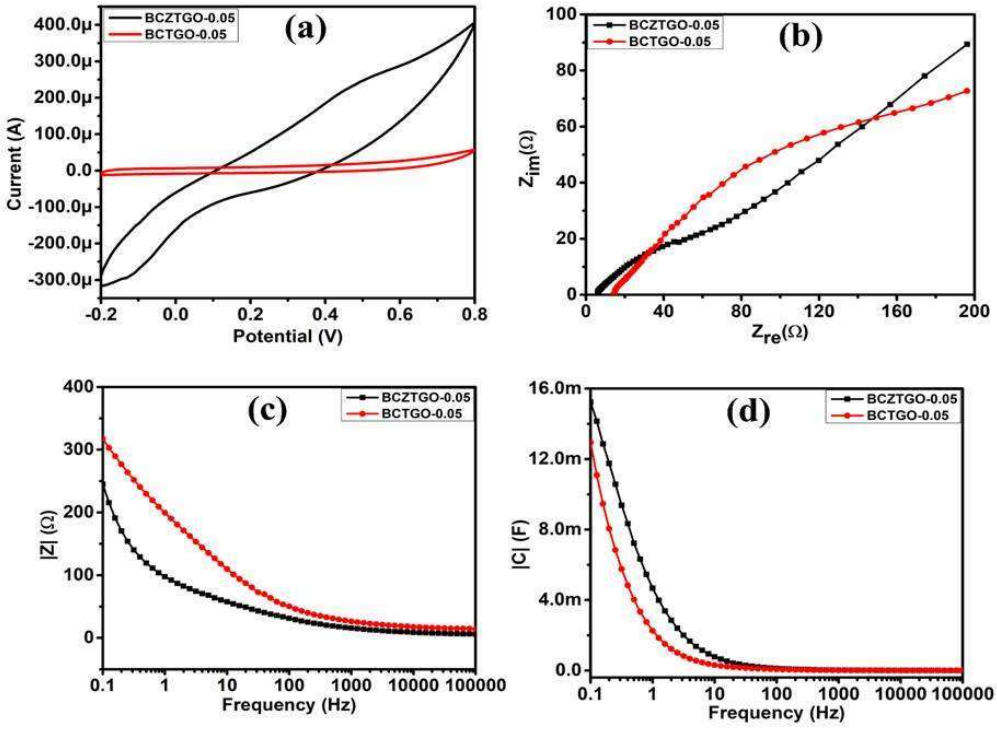

Fig. 6.11(a) Cyclic voltammetry, (b) Nyquist plot, (c) Frequency vs total impedance plot, (d) Frequency vs net capacitance plot of BCZTGO-0.05 and BCTGO-0.05 ceramics

The specific capacitance of BCZTGO-0.05 and BCTGO-0.05 were found to be 15.7 F/g and 13.05 F/g, respectively. Resistances given by various constituents in the electrochemical systems were obtained from electrochemical impedance spectroscopy (EIS). In the real Z axis of the Nyquist plot, the intercept point gives the value of equivalent series resistance (R_S). R_S is the contribution of resistances obtained from electrolyte or solution, current collector and electrode, intrinsic resistance present in the composite, and chemically inactive components of the composite. The semicircular diameter in the Nyquist plot exhibits charge transfer resistance (R_{CT}), which is the reason for obstruction in faradaic transitions and charge mobility in the time of electrochemical reactions [26]. BCZTGO-0.05 and BCTGO-

0.05 have charge transfer resistances of 70 Ω and 192 Ω, respectively (Fig. 6.11b and **Fig**. 6.11c)exhibits that with the increase in frequency, the impedance is decreasing for both low and high frequency. With the increase in frequency, the mobility of electrolyte ions increases resulting less impedance. Fig. 6.11d exhibits a decreasing trend of capacitance with increase in frequency, which could be due to the incomplete transitions and less residence time of the electrolyte ions during electrochemical reactions [27].

6.4. Conclusions

$Bi_{2/3}Cu_3Ti_{4-x}Ge_xO_{12}$ and $Bi_{2/3}Cu_{3-x}Zn_xTi_{4-x}Ge_xO_{12}$ (where x= 0.05) ceramics were successfully synthesized by semi-wet route and sintered at 1123 K for 8 h. Phase formation of these ceramics was confirmed by XRD. The crystallite size of BCTGO-0.05 and BCZTGO-0.05 ceramics were in the range of 39-47 nm. The particle size of BCTGO-0.05and BCZTGO-0.05 ceramics were found as 99 ± 5 and 112 ± 10 nm. The oxidation state was validated by XPS. The dielectric constant for BCTGO-0.05 ceramic was found as 563 at 100 Hz and 423 K. For the BCZTGO-0.05 ceramic, the tangent loss at 303 K temperature and 10 kHz frequency was 0.18.The conductivity variation of BCTGO-0.05 and BCZTGO-0.05 ceramics with temperature support the Arrhenius law in the temperature range 300-500 K. AC conductivity of BCTGO-0.05 and BCZTGO-0.05 ceramics increase with increasing frequency satisfying Johncher's power law. The specific capacitance of BCTGO-0.05 and BCZTGO-0.05 were found to be 13.05 F/g and 15.7 F/g, respectively.

References:

[1] Behera, C., Patel, P., Pradhan, N. and Choudhary, R.N.P. (2022). Studies of structural, dielectric and electrical characteristics of nickel-modified barium titanate for device applications. *Journal of Materials Science: Materials in Electronics*, 33(3), 1657-1669.

[2] Boruah, B.D. (2021). Recent advances in off-grid electrochemical capacitors. *Energy Storage Materials*, 34, 53-75.

[3] Mohd Aman, A.H., Shaari, N. and Ibrahim, R. (2021). Internet of things energy system: Smart applications, technology advancement, and open issues. *International Journal of Energy Research*, 45(6), 8389-8419.

[4] Xu, D., Yue, X., Zhang, Y., Song, J., Chen, X., Zhong, S., Ma, J., Ba, L., Zhang, L. and Du, S. (2019). Enhanced dielectric properties and electrical responses of cobalt-doped $CaCu_3Ti_4O_{12}$ thin films. *Journal of Alloys and Compounds*, 773, 853-859.

[5] Boonlakhorn, J., Chanlek, N., Manyam, J., Srepusharawoot, P., Krongsuk, S. and Thongbai, P. (2021). Enhanced giant dielectric properties and improved nonlinear electrical response in acceptor-donor (Al^{3+}, Ta^{5+})-substituted $CaCu_3Ti_4O_{12}$ ceramics. *Journal of Advanced Ceramics*, 10, 1243-1255.

[6] Chao, X., Wu, P., Zhao, Y., Liang, P. and Yang, Z. (2015). Effect of $CaCu_3Ti_4O_{12}$ powders prepared by the different synthetic methods on dielectric properties of $CaCu_3Ti_4O_{12}$/polyvinylidene fluoride composites. *Journal of Materials Science: Materials in Electronics*, 26, 3044-3051.

[7] Zhang, C., Wang, Y., Chen, Y., Wang, Y., Wang, P. and Wu, Q. (2022). A Novel Method to Synthesize Co/Fe_3O_4 Nanocomposites with Optimal Magnetic and Microwave Performance. *Nanomaterials*, 12(16), 2764.

[8] Li, M., Shen, Z., Nygren, M., Feteira, A., Sinclair, D.C. and West, A.R. (2009). Origin (s) of the apparent high permittivity in $CaCu_3Ti_4O_{12}$ ceramics: clarification on the contributions from internal barrier layer capacitor and sample-electrode contact effects. *Journal of Applied Physics*, 106(10), 104106.

[9] Xiao, M., Li, L. and Zhang, P. (2018). Non-Ohmic properties of $MgTiO_3$ doped $CaCu_3Ti_4O_{12}$ thin films deposited by magnetron sputtering method. *Journal of Alloys and Compounds*, 743, 570-575.

[10] Neepamala, G., Archita, M., Sanchari, S. and Ray, R. (2020). Doping-induced dielectric and transport properties of $Ni_{1-x}Zn_xO$. *Journal of Materials Science. Materials in Electronics*, 15, 12628-12637.

[11] Boonlakhorn, J., Manyam, J., Srepusharawoot, P., Krongsuk, S. and Thongbai, P. (2021). Effects of charge compensation on colossal permittivity and electrical properties of grain boundary of $CaCu_3Ti_4O_{12}$ ceramics substituted by Al3+ and $Ta^{5+/}Nb^{5+}$. *Molecules*, 26(11), 3294.

[12] Tan, Y.Q., Zhang, J.L., Hao, W.T., Chen, G., Su, W.B. and Wang, C.L. (2010). Giant dielectric-permittivity property and relevant mechanism of $Bi_{2/3}Cu_3Ti_4O_{12}$ ceramics. *Materials Chemistry and Physics*, 124(2-3), 1100-1104.

[13] Ahmad, M.M., Alshoaibi, A., Ansari, S.A., Kayed, T.S., Khater, H.A. and Kotb, H.M. (2022). Dielectric Properties of $Bi_{2/3}Cu_3Ti_4O_{12}$ Ceramics Prepared by Mechanical Ball Milling and Low Temperature Conventional Sintering. *Materials*, 15(9), 3173.

[14] Hargreaves, J.S.J. (2016). Some considerations related to the use of the Scherrer equation in powder X-ray diffraction as applied to heterogeneous catalysts. *Catalysis, Structure & Reactivity*, 2(1-4), 33-37.

[15] Imam, N.G., Aquilanti, G., Azab, A.A. and Ali, S.E. (2021). Correlation between structural asymmetry and magnetization in Bi-doped $LaFeO_3$ perovskite: a combined XRD and synchrotron radiation XAS study. *Journal of Materials Science: Materials in Electronics*, 32, 3361-3376.

[16] Huang, Y., Wu, K., Xing, Z., Zhang, C., Hu, X., Guo, P., Zhang, J. and Li, J. (2019). Understanding the validity of impedance and modulus spectroscopy on exploring electrical heterogeneity in dielectric ceramics. *Journal of Applied Physics*, *125*(8), 084103.

[17] Kumar, R., Zulfequar, M. and Senguttuvan, T.D. (2019). Improved giant dielectric properties in microwave flash combustion derived and microwave sintered $CaCu_3Ti_4O_{12}$ ceramics. *Journal of Electroceramics*, 42, 41-46.

[18] Tallapally, V., Nakagawara, T.A., Demchenko, D.O., Özgür, Ü. and Arachchige, I.U. (2018). $Ge_{1-x}Sn_x$ alloy quantum dots with composition-tunable energy gaps and near-infrared photoluminescence. *Nanoscale*, 10(43), 20296-20305.

[19] Ren, L., Yang, L., Xu, C., Zhao, X. and Liao, R. (2018). Improvement of breakdown field and dielectric properties of $CaCu_3Ti_4O_{12}$ ceramics by Bi and Al co-doping. *Journal of Alloys and Compounds*, 768, 652-658.

[20] Mansour, S.F., Imam, N.G., Goda, S. and Abdo, M.A. (2020). Constructive coupling between $BiFeO_3$ and $CoFe_2O_4$; promising magnetic and dielectric properties. *Journal of Materials Research and Technology*, 9(2), 434-1446.

[21] Han, C.S., Choi, H.R., Choi, H.J. and Cho, Y.S. (2017). Origin of abnormal dielectric behavior and chemical states in amorphous $CaCu_3Ti_4O_{12}$ thin films on a flexible polymer substrate. *Chemistry of Materials*, 29(14), 5915-5921.

[22] Alcántar-Vázquez, B., Díaz Herrera, P.R., Barrera González, A., Duan, Y. and Pfeiffer, H. (2015). Analysis of the CO_2–H_2O chemisorption in lithium silicates at low temperatures (30–80 C). *Industrial & Engineering Chemistry Research*, 54(27), 6884-6892.

[23] Rai, V.S., Prajapati, D., Verma, M.K., Kumar, V., Pandey, S., Das, T., Singh, N.B. and Mandal, K.D. (2022). Influence of Zn doping on microstructure, dielectric, and electric properties in $Bi_{2/3}Cu_3Ti_4O_{12}$ ceramic synthesized by the semi-wet method. *Journal of Materials Science: Materials in Electronics*, 33(18), 14868-14881.

[24] Dhavala, L., Bhimireddi, R., Kollipara, V.S. and Varma, K.B. (2023). Exceptional dielectric and varistor properties of Sr, Zn and Sn co-doped calcium copper titanate ceramics. *RSC advances*, 13(16), 10476-10487.

[25] Das, T. and Verma, B. (2020). Effect of ruthenium based catalyst loading on the electrochemical properties of carbon xerogel. *Chemical Physics Letters*, 739, 136947.

[26] Das, T. and Verma, B. (2020). Polyaniline-Acetylene black-Copper cobaltite based ternary hybrid material with enhanced electrochemical properties and its use in supercapacitor electrodes. *International Journal of Energy Research*, 44(2), 934-949.

[27] Das, T. and Verma, B. (2022). Novel S-doped polyaniline@ $CuCo_2O_4$–carbon composites and optimization of their weight ratios on the basis of their electrochemical activities. *Polymer-Plastics Technology and Materials*, 61(5), 516-531.

[28] Prajapati, D., Rai, V.S., Pandey, S., Kumar, V., Verma, M.K., Kumar, A., Singh, S., Sahoo, K. and Mandal, K.D. (2021). Studies of microstructural, dielectric, and impedance

spectroscopic properties of $Bi_{0.617}Y_{0.05}Cu_3Ti_4O_{12}$ ceramic synthesized through semi-wet route. *Journal of Materials Science: Materials in Electronics*, 32, 26371-26383.

[29] Mohammed, J., Bhargava, R., Khan, S., Mishra, S., Godara, S.K. and Srivastava, A.K. (2020). Crystal structure refinement, optical properties, dielectric response, and impedance spectroscopy of Ni^{2+}-Co^{2+} substituted bismuth copper titanate (BCTO). *Materials Chemistry and Physics*, 248, 122933.

[30] Mondal, K. and Sharma, A. (2016). Recent advances in electrospun metal-oxide nanofiber based interfaces for electrochemical biosensing. *RSC advances*, 6(97), 94595-94616.

[31] Musahwar, N., Khan, M.M., Husain, M. and Zulfequar, M., 2007. Electrical conductivity and relaxation of Se–S–In glasses. *Journal of Physics D: Applied Physics*, 40(24), 7787.